Quantitative scanning microwave microscopy of 2D electron and hole gases in AlN/GaN heterostructures

View Online   Export Citation   CrossMark

Xiaopeng Wang,[1,a] (ID) Gianluca Fabi,[2] Reet Chaudhuri,[1] (ID) Austin Hickman,[1] Mohammad Javad Asadi,[1]
Kazuki Nomoto,[1] Huili Grace Xing,[1,3] (ID) Debdeep Jena,[1,3] (ID) Marco Farina,[2] (ID) and James C. M. Hwang[1,3]

AFFILIATIONS

[1]School of Electrical and Computer Engineering, Cornell University, Ithaca, New York 14853, USA
[2]Department of Information Engineering, Marche Polytechnic University, Ancona 60131, Italy
[3]Department of Materials Science and Engineering, Cornell University, Ithaca, New York 14853, USA

Note: This paper is part of the APL Special Collection on Wide- and Ultrawide-Bandgap Electronic Semiconductor Devices.
[a]Author to whom correspondence should be addressed: xw569@cornell.edu

ABSTRACT

Although the scanning microwave microscope (SMM) is based on the atomic force microscope (AFM), the SMM differs from the AFM by being able to sense subsurface electromagnetic properties of a sample. This makes the SMM promising for in-depth nondestructive characterization of nanoelectronic structures. However, the SMM raw data are convoluted with the sample topography, making it especially challenging for quantitative characterization of nonplanar structures. In this paper, using the topography information simultaneously obtained by the AFM and the *in situ* extracted probe geometry, we de-embed from the topography-corrupted SMM data the sheet resistance of 2D electron or hole gas (2DEG or 2DHG) buried at the interface of an AlN/GaN heterostructure, including the lateral depletion of the 2DEG from an etched step. The SMM results are validated by Hall-effect measurements. The limitation and possible improvement in the present technique are discussed. With improved setup, the SMM can be used to nondestructively monitor the local sheet resistance of 2DEG or 2DHG during device manufacture. These studies help to pave the way to 3D microwave tomography on the nanometer scale.

Published under an exclusive license by AIP Publishing. https://doi.org/10.1063/5.0072358

Based on a scanning nanoprobe in near-field electromagnetic interaction with the sample, a scanning microwave microscope (SMM) can have nanometer spatial resolution similar to that of an atomic force microscope (AFM),[1–5] despite the centimeter-long microwave. Different from the AFM, the SMM is sensitive to subsurface electromagnetic properties of a sample and is promising for in-depth nondestructive characterization of nanoelectronic structures.[6–9] However, the SMM raw data are convoluted with the sample topography, making it especially challenging for quantitative characterization of nonplanar structures.[10,11] In this paper, using the topography information simulaneously obtained by the AFM and the *in situ* extracted probe geometry, we overcome the challenge to de-embed from the topography-corrupted SMM data the sheet resistance of 2D electron or hole gas (2DEG or 2DHG) buried at the interface of an AlN/GaN heterostructure. The results are validated by Hall-effect measurements on other chips from the same wafers.

For proof of principle, AlN/GaN heterostructures are chosen, because the 2DEG or 2DHG can be induced at the interface by polarization alone without dopant ions to impede the SMM signal.[12,13] Additionally, AlN and GaN have similar dielectric constants (8.5 and 8.9, respectively),[14] which simplifies simulation and analysis. Technologically, 2DEG and 2DHG AlN/GaN heterostructures are the foundations of *n*- and *p*-type GaN field-effect transistors. The former is key to high-power microwave and millimeter-wave amplifiers;[15] the latter is critical to push-pull analog amplifiers and complementary logic based on wide-bandgap semiconductors.[16]

Figure 1 illustrates schematically the three types of AlN/GaN heterostructures used: (a) a flat 2DEG heterostructure, (b) a patterned 2DEG heterostructure, and (c) a patterned 2DHG heterostructure (the supplementary material, sample preparation). All layer compositions and thicknesses are verified by *x*-ray diffraction leaving unknown the sheet resistance of the 2DEG or 2DHG. Although the sheet resistance
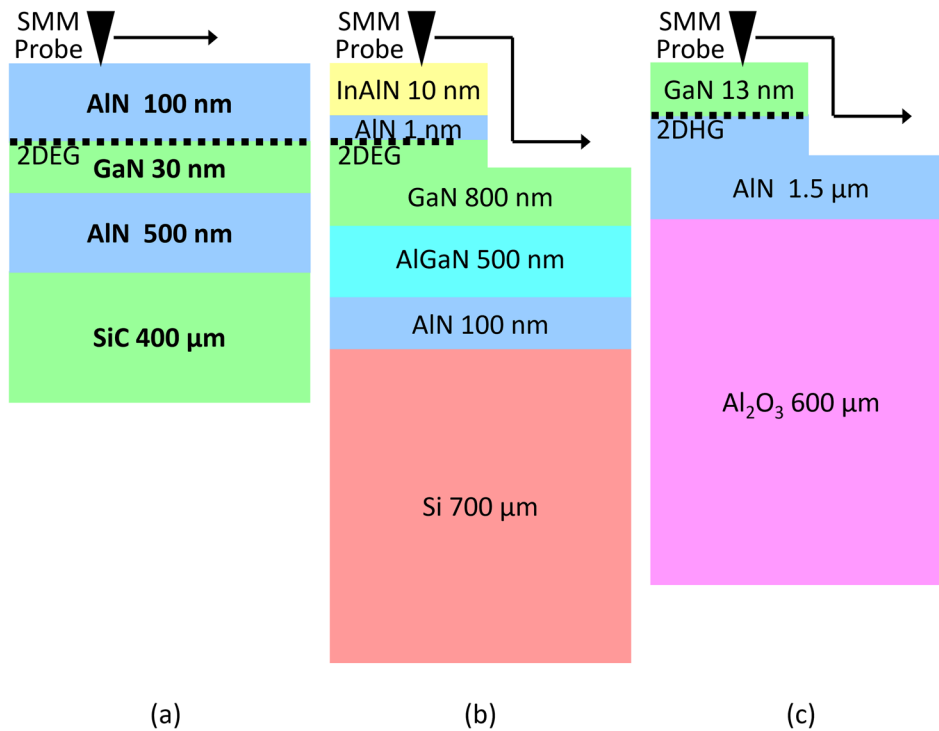
FIG. 1. (a) Flat 2DEG, (b) patterned 2DEG, and (c) patterned 2DHG heterostructures.

can be characterized by the Hall-effect measurement, it may differ from that of the actual device after fabrication. As part of device fabrication, the active regions of 2DEG and 2DHG are isolated by selective-area ion bombardment (10^{15} cm^{-2} N at 35 keV) or BCl$_3$-based plasma etching. The former results in a flat surface; the latter results in steps of 39 and 200 nm on the 2DEG and 2DHG heterostructures, respectively. Both flat and patterned heterostructures are scanned at 6.2 GHz, a trade-off between sensitivity and signal-to-noise ratio. The scanned data are compared with that simulated with the sheet resistance of the 2DEG or 2DHG as a fitting parameter. In the simulation, the 2DEG or 2DHG region is treated as a pure conductor, with the remaining heterostructure treated as a pure insulator. To further simplify the simulation, the dielectric constant of GaN, AlGaN, or InAlN is assumed to be the same as that of AlN. Similarly, the dielectric constant of AlN is assumed to be the same before and after ion bombardment. The difference from using precise dielectric constants for the different layers is negligible (suplementary material, simulated effect of permittivity difference between AlN and GaN). Although the metal probe forms a Schottky contact with AlN and GaN, the effect of the Schottky barrier on these wide-bandgap semiconductors is negligible (suplementary material, simulated effect of schottky barrier).

The SMM probe, while in contact with the sample, is scanned across the sample surface by a piezoelectric stage, so that AFM and SMM signals can be obtained simultaneously (supplementary material, measurement setup). The basic calibration procedure is conventional and briefly summarized here.[17,18] The AFM signal, calibrated by a 110-nm-thick grating, determines the sample topography. The SMM signal, defined as the complex reflection coefficient S_{11} and calibrated *in situ* by "short" and "open" standards,[17] determines the probe-

sample interaction conductance and capacitance after de-embedding the effects of cables and connectors.[18] "Short" is achieved by contacting the probe with the metal sample holder next to the sample chip. "Open" is achieved by lifting the probe 3 μm above the sample holder. In between, the height (z) dependence of the interaction capacitance as calibrated by operating the AFM in the electrostatic force mode[19] is used to extract the probe geometry, which may vary with usage.[20,21] As illustrated in Fig. 2(a), the probe geometry is modeled by a half ball attached to a truncated cone, which is in turn attached to a cantilever. For the present probe, the ball radius $r = 0.95 \mu$m, the half-cone angle $\theta = 33°$, and the cone height $h = 55 \mu$m. The ball radius is a trade-off between sensitivity and spatial resolution. The slender cone of the probe minimizes the cantilever capacitance. Figures 2(b) and 2(c) are discussed after Fig. 4 is discussed.

It is commonly assumed that the topography effect on the total interaction capacitance, including that of the ball (C_{BALL}), cone (C_{CONE}), and cantilever (C_{CANTI}), is a function of z only.[10,21] This allows the topography effect to be corrected by the z values measured by the AFM. However, when the topographic feature size (e.g., step height) approaches the probe size (r), C_{BALL} and C_{CONE} can also be functions of the lateral distances x and y from the feature. Therefore, in this work, we use 3D COMSOL to simulate the topography effect on C_{BALL} and C_{CONE} as the probe scans across an active region of 2DEG or 2DHG (supplementary material, simulation method). The topography effect on C_{CANTI} is neglected, because, with the slender cone, it is estimated to be on the order of 0.01 fF and much smaller than the total capacitance contrast induced by the 2DEG or 2DHG as shown in Figs. 3–5. These figures also show agreement between simulation and measurement. Later, in the discussion of Fig. 4, it will be shown that by considering the probe size relatively to a step height
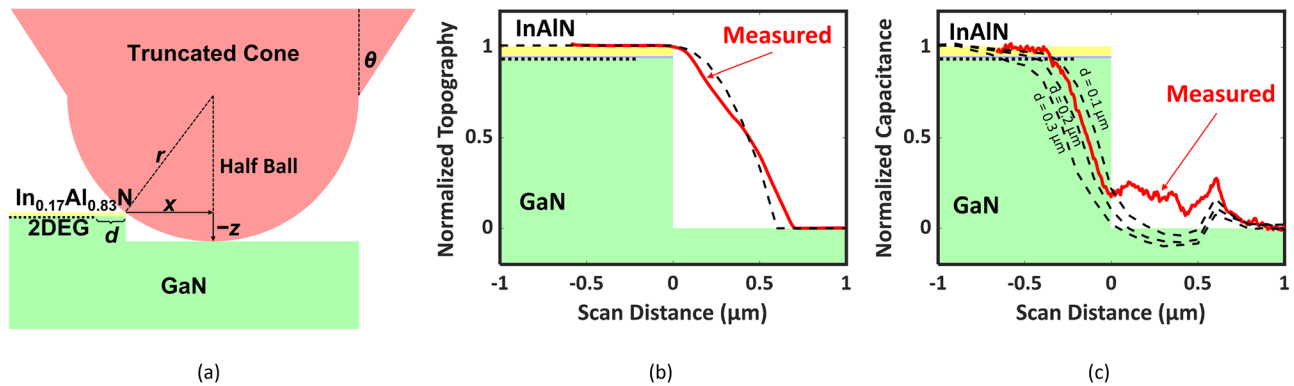
FIG. 2. (a) Probe schematic and (b) normalized line profile of AFM topography scan, and (c) normalized line profile of SMM capacitance contrast of a patterned 2DEG hetero-structure with the 2DEG depleted by d from the edge. Dashed curves are simulated.

and its lateral distances x and y from the step, we can determine the depletion width of the 2DEG from the step.

Figures 3 shows the AFM topography image and SMM interaction conductance and capacitance images for the flat 2DEG heterostructure [Fig. 1(a)]. It can be seen in Fig. 3(a) that the AFM image is featureless except atomic steps of 0.3 nm. By contrast, the 2DEG

region is distinguishable in the SMM images by average conductance contrast of 0.47 ± 0.3 μS and capacitance contrast of 0.18 ± 0.03 fF with respective to the isolated region. These contrasts are averaged from the x-y line scans across the images of Figs. 3(c) and 3(d) (supplementary material, line profiles). These measured contrasts are consistent with that simulated as illustrated in Fig. 3(b). However, the
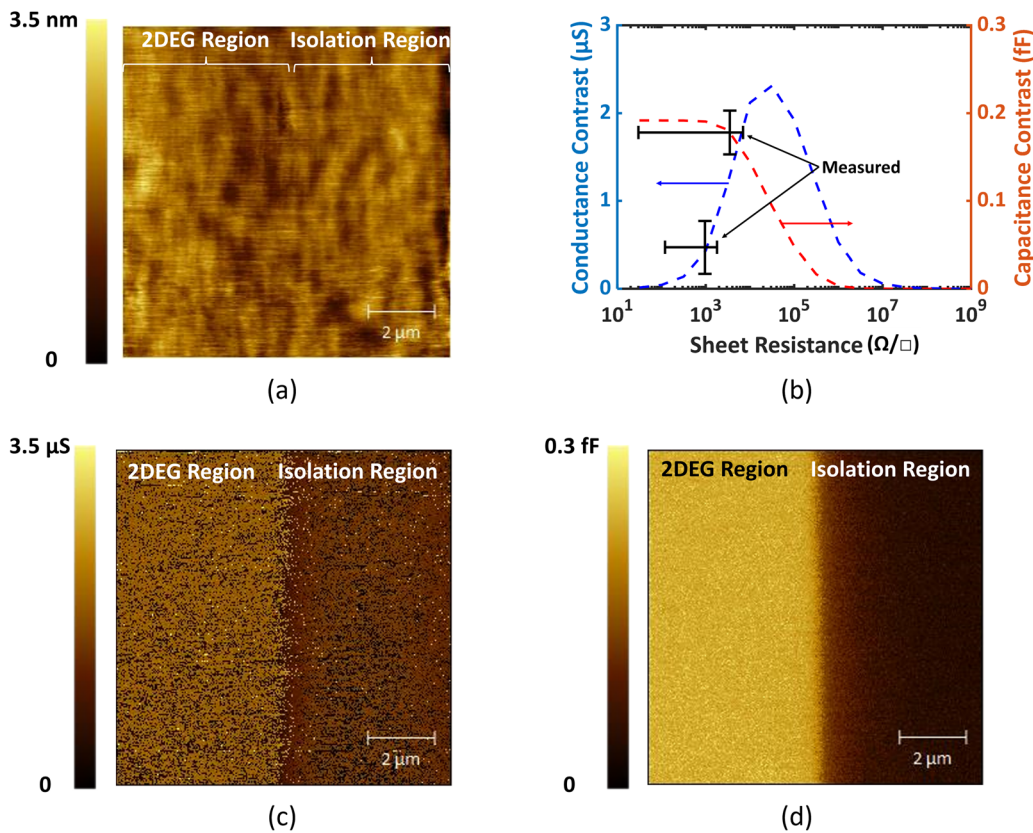

FIG. 3. (a) AFM topography image, (b) SMM conductance/capacitance contrasts, (c) SMM conductance image, and (d) SMM capacitance image of a flat 2DEG heterostructure [Fig. 1(a)]. Dashed curves are simulated.
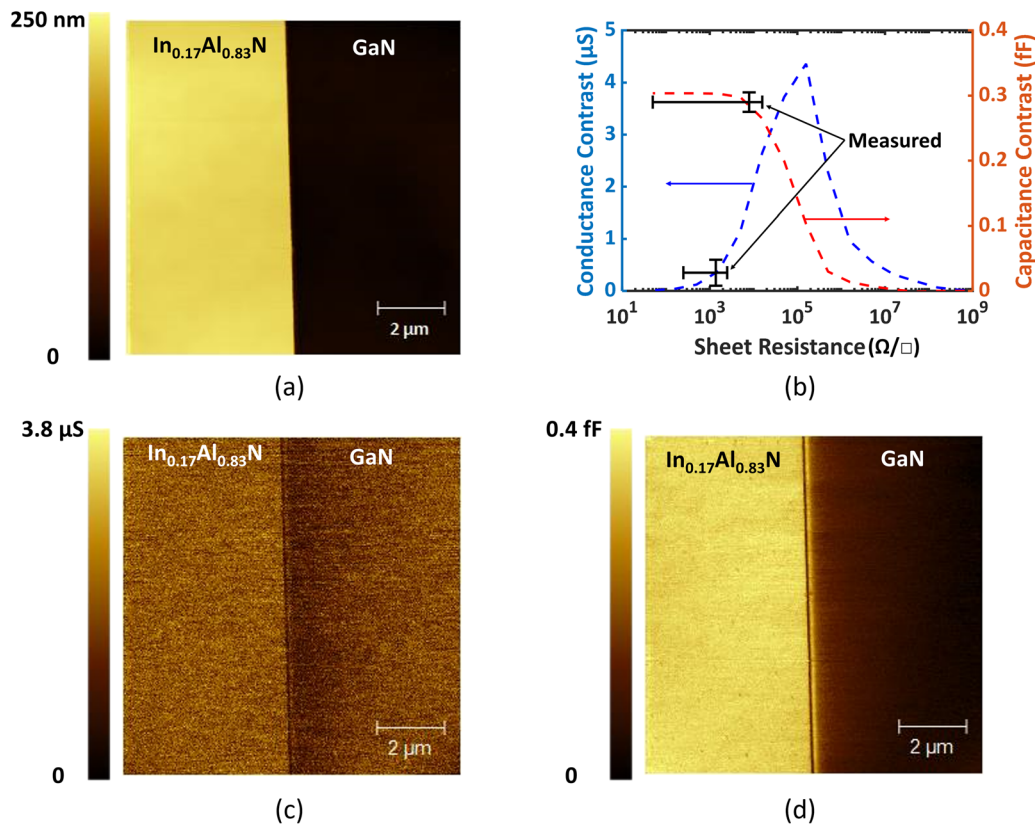
FIG. 4. (a) AFM topography image, (b) SMM conductance/capacitance contrasts, (c) SMM conductance image, and (d) SMM capacitance image of a patterned 2DEG heterostructure [Fig. 1(b)]. Dashed curves are simulated.

conductance contrast can narrow down the range of the 2DEG sheet resistance to $960 \pm 840 \, \Omega/\square$, in general agreement with the Hall-measured value of $450 \, \Omega/\square$. The uncertainty in sheet resistance is enlarged by the relatively weak dependence of the conductance contrast on the sheet resistance around $1 \, k\Omega/\square$. Had a higher frequency been used to make the dependence steeper around $1 \, k\Omega/\square$, the uncertainty in sheet resistance can be reduced (supplementary material, simulated effect of SMM frequency). By contrast, although the capacitance contrast can have a relatively small uncertainty ($0.18 \pm 0.03 \, fF$), its dependence on the sheet resistance around $1 \, k\Omega/\square$ is rather flat, making it even less certain to determine the sheet resistance from the capacitance contrast. Nevertheless, the above result demonstrates the SMM's below-surface sensitivity to electrical features not detectable by the AFM.[22] The SMM precision can be improved by using a higher frequency, which shifts the sensitive region to lower sheet resistance (Fig. S5).

Figure 4 shows that the active region of the patterned 2DEG heterostructure [Fig. 1(b)] is distinguishable in not only the SMM conductance/capacitance images, but also the AFM topography image as expected. As the probe scans from the $In_{0.17}Al_{0.83}N$ mesa down to the GaN region, the average contrast is $200 \pm 6 \, nm$ in topography, $0.35 \pm 0.25 \, \mu S$ in conductance, and $0.29 \pm 0.02 \, fF$ in capacitance. Comparing the measured and simulated conductance/capacitance contrasts, the conductance contrast can again narrow down the 2DEG

sheet resistance range to $1.4 \pm 1.1 \, k\Omega/\square$, which is higher than the Hall-measured value of $200 \, \Omega/\square$. The reason for the discrepancy needs to be further investigated. Upon close examination, it can be seen that the contrast between $In_{0.17}Al_{0.83}N$ and GaN is sharp in the AFM image, but an extra fringe beyond the edge is present in the SMM images. The extra SMM fringe can be explained by the finite SMM probe size compared to the step height. As illustrated in Fig. 2(b), when the probe starts to roll-off the edge, its overlap with the 2DEG decreases and so does the interaction capacitance. However, when the probe just lands on GaN, its side contacts the 2DEG edge, resulting in a local peak in the capacitance and an extra fringe in the image. The height of this peak and the depth of the valley before the peak may be modulated by the 2DEG depletion width d from the edge as indicated by the simulated $C(x)$ characteristics shown in Fig. 2(c). Comparing the simulated and measured data, it is estimated that $d \approx 0.2 \, \mu m$. This shows that SMM can be used to quantify not only the sheet resistance of the 2DEG, but also the depletion width of the 2DEG from the etched step.

Similar to Fig. 4, Fig. 5 shows that the active region of the patterned 2DHG heterostructure [Fig. 1(c)] is distinguishable in not only the SMM conductance/capacitance images, but also the AFM topography image. As the probe scans from the GaN mesa down to the AlN region, the average contrast is $39 \pm 2 \, nm$ in topography, $2.8 \pm 0.7 \, \mu S$ in conductance, and $0.23 \pm 0.02 \, fF$ in capacitance. It can be seen that
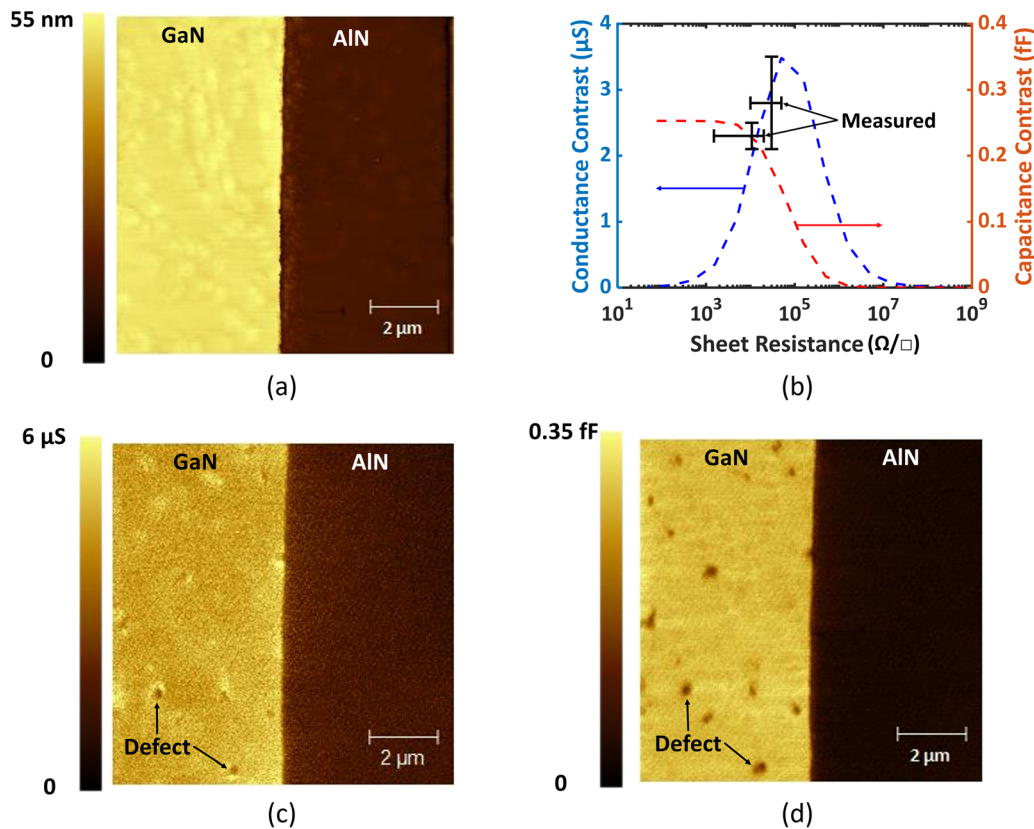
FIG. 5. (a) AFM topography image, (b) SMM conductance/capacitance contrasts, (c) SMM conductance image, and (d) SMM capacitance image of a patterned 2DHG heterostructure [Fig. 1(c)]. Dashed curves are simulated.

the higher sheet resistance of the 2DHG makes it more sensitive to the SMM conductance contrast, so that it is more accurately determined to be $13 \pm 5\,\text{k}\Omega/\square$, which agrees with the $15\,\text{k}\Omega/\square$ value of the Hall measurement. Compared to Fig. 4, the SMM images of the 2DHG do not show any extra fringe near the etched step, probably because the step height of 39 nm is much smaller than the probe radius. On the other hand, the SMM images show defect spots that are absent in the AFM image. These defects appear darker, indicating higher resistance than the surrounding 2DHG. The defect density is approximately $3 \times 10^7\,\text{cm}^{-2}$, which is orders-of-magnitude lower than the typical threading dislocation density in AlN and GaN layers grown on foreign substrates, such as Si, SiC, and Al_2O_3.[23] This suggests that not all dislocations are electrically active.[24] The nature of these defects needs to be better characterized, because they can be scattering centers for mobile holes.

In conclusion, the SMM-measured sheet resistances of the 2DEG and 2DHG in AlN/GaN heterostructures are generally consistent with Hall-measured values, whether the heterostructure is flat or not. The extra fringe in a patterned 2DEG heterostructure is attributable to the depletion of the 2DEG from the etched step. Defects that are more resistive in SMM images of a patterned 2DHG heterostructure suggest that not all dislocations are electrically active. The SMM sensitivity can be improved by using a much higher frequency (presently limited to 10 GHz) or an inverted SMM.[25] Modifying the present setup for an inverted SMM can greatly extend the bandwidth and the dynamic range because the inverted SMM can measure the transmission coefficient in addition to the reflection coefficient. With improved sensitivity, the SMM may be used to nondestructively monitor the local sheet resistance of 2DEG or 2DHG in actual device structure during fabrication.[26] Presently, the SMM characterizes the sheet resistivity but not the carrier type. The carrier type (2DEG vs 2DHG) is inferred from the band diagram and confirmed by the Hall measurement. If necessary, a DC bias can be added to the SMM microwave signal, and, by detecting the increase or decrease in the sheet resistance under a positive or negative bias, SMM can also confirm the carrier type and the 2DEG/2DHG electrostatics.

See the supplementary material for sample preparation, measurement setup, simulation method, line profiles, simulated effect of SMM frequency, simulated effect of permittivity difference between AlN and GaN, and simulated effect of Schottky barrier.[27]

AUTHOR DECLARATIONS
Conflict of Interest

The authors have no conflicts to disclose.

DATA AVAILABILITY

The data that support the findings of this study are available from the corresponding author upon reasonable request.

REFERENCES

[1] R. C. Chintala, K. Rubin, and Y. Yang, IEEE Microwave Mag. **21**, 22 (2020).
[2] S. Berweger, T. M. Wallis, and P. Kabos, IEEE Microwave Mag. **21**, 36 (2020).
[3] M. Farina and J. C. M. Hwang, IEEE Microwave Mag. **21**, 52 (2020).
[4] L. Zheng, L. Shao, M. Loncar, and K. Lai, IEEE Microwave Mag. **21**, 60 (2020).
[5] A. Tselev, IEEE Microwave Mag. **21**, 72 (2020).
[6] K. Lai, W. Kundhikanjana, M. A. Kelly, Z. Shen, J. Shabani, and M. Shayegan, Phys. Rev. Lett. **107**, 176809 (2011).
[7] E. Y. Ma, M. R. Calvo, J. Wang, B. Lian, M. Mühlbauer, C. Brüne, Y. Cui, K. Lai, W. Kundhikanjana, Y. Yang, M. Baenninger, M. König, C. Ames, H. Buhmann, P. Leubner, L. W. Molenkamp, S. Zhang, D. Goldhaber-Gordon, M. A. Kelly, and Z. Shen, Nat. Commun. **6**, 7252 (2015).
[8] W. Choi, E. Seabron, P. K. Mohseni, J. D. Kim, T. Gokus, A. Cernescu, P. Pochet, H. T. Johnson, W. L. Wilson, and X. Li, ACS Nano **11**, 1530 (2017).
[9] M. Allen, Y. Cui, E. Y. Ma, M. Mogi, M. Kawamura, I. C. Fulga, D. Goldhaber-Gordon, Y. Tokura, and Z. Shen, Proc. Natl. Acad. Sci. U. S. A. **116**, 29 (2019).
[10] M. C. Biagi, R. Badino, R. Fabregas, G. Gramse, L. Fumagalli, and G. Gomila, Phys. Chem. Chem. Phys. **19**, 3884 (2017).
[11] G. Fabi, C. H. Joseph, E. Pavoni, X. Wang, R. Al Hadi, J. C. M. Hwang, A. Morini, and M. Farina, IEEE Trans. Microwave Theory Tech. **69**, 2662 (2021).
[12] F. Bernardini, V. Fiorentini, and D. Vanderbilt, Phys. Rev. B **56**, R10024 (1997).
[13] R. Chaudhuri, S. J. Bader, Z. Chen, D. A. Muller, H. G. Xing, and D. Jena, Science **365**, 1454 (2019).
[14] R. Quay, *Gallium Nitride Electronics* (Springer, Freiburg, 2008).
[15] A. Hickman, R. Chaudhuri, L. Li, K. Nomoto, S. J. Bader, J. C. M. Hwang, H. G. Xing, and D. Jena, IEEE J. Electron Devices Soc. **9**, 121 (2021).
[16] S. J. Bader, H. Lee, R. Chaudhuri, S. Huang, A. Hickman, A. Molnar, H. G. Xing, D. Jena, H. W. Then, N. Chowdhury, and T. Palacios, IEEE Trans. Electron Devices **67**, 4010 (2020).
[17] M. Farina, D. Mencarelli, A. D. Donato, G. Venanzoni, and A. Morini, IEEE Trans. Microwave Theory Tech. **59**, 2769 (2011).
[18] G. Gramse, A. Kölker, T. Lim, T. J. Z. Stock, H. Solanki, S. R. Schofield, E. Brinciotti, G. Aeppli, F. Kienberger, and N. J. Curson, Sci. Adv. **3**(6), e1602586 (2017).
[19] G. Gramse, M. Kasper, L. Fumagalli, G. Gomila, P. Hinterdorfer, and F. Kienberger, Nanotechnology **25**, 145703 (2014).
[20] X. Jin, J. C. M. Hwang, D. Mencarelli, L. Pierantoni, and M. Farina, IEEE Microwave Mag. **18**, 71 (2017).
[21] X. Jin, M. Farina, X. Wang, G. Fabi, X. Cheng, and J. C. M. Hwang, IEEE Trans. Microwave Theory Tech. **67**, 5438 (2019).
[22] X. Jin, K. Xiong, R. Marstell, N. C. Strandwitz, J. C. M. Hwang, M. Farina, A. Göritz, M. Wietstruck, and M. Kaynak, Int. J. Microwave Wireless Technol. **10**, 556 (2018).
[23] Y. Cao, Semicond. Semimetals **102**, 41 (2019).
[24] S. Usami, A. Tanaka, H. Fukushima, Y. Ando, M. Deki, S. Nitta, Y. Honda, and H. Amano, Jpn. J. Appl. Phys., Part 1 **58**, SCCB24 (2019).
[25] M. Farina, X. Jin, G. Fabi, E. Pavoni, A. di Donato, D. Mencarelli, A. Morini, F. Piacenza, R. A. Hadi, Y. Zhao, Y. Ning, T. Pietrangelo, X. Cheng, and J. C. M. Hwang, Appl. Phys. Lett. **114**, 093703 (2019).
[26] R. Chaudhuri, S. J. Bader, Z. Chen, D. Muller, H. G. Xing, and D. Jena, Phys. Status Solidi B **257**, 1900567 (2020).
[27] L. Li, K. Nomoto, M. Pan, W. Li, A. Hickman, J. Miller, K. Lee, Z. Hu, S. J. Bader, S. M. Lee, J. C. M. Hwang, D. Jena, and H. G. Xing, IEEE Electron Device Lett. **41**, 689 (2020).